CrossMark

ARTICLE

A chemomechanical coupling model for oxidation and stress evolution in ZrB_2–SiC

Hailong Wang and Shengping Shen[a)]
State Key Laboratory for Strength and Vibration of Mechanical Structures, School of Aerospace, Xi'an Jiaotong University, Xi'an 710049, China

(Received 19 September 2016; accepted 28 November 2016)

A chemomechanical coupling model is presented in the temperature range of 1200–1800 °C based on the microstructure during oxidation of ZrB_2–SiC. The model includes the interaction of the oxidation rate and the mechanical stress. The stress is generated due to the constraint from the substrate to the lateral growth. The generated stress results in the shrink of the pores in the oxide. At the outer glassy layer surface, the boundary layer evaporation is adopted to describe the evaporation rate. Using the coupling model, the evolutions of the oxide layer thickness, weight gain, pore radius, and stress in both the oxide and substrate are provided, and the theoretical calculated results agree well with the reported experimental results. The results reveal large stress in the oxide layer during the oxidation process. By comparing the results of ZrB_2 with different volume fractions of SiC, it is found that ZrB_2 with higher volume fraction of SiC has more excellent oxidation resistance and smaller stress.

I. INTRODUCTION

Transition metal diborides, especially ZrB_2 and HfB_2, have high melting temperature, high thermal conductivity and excellent oxidation resistance, which makes ultrahigh temperature ceramics (UHTCs) be the most promising candidates used in the re-entry and hypersonic vehicles as leading edge components.[1–7] Moreover, within the family of UHTCs, ZrB_2 has the lowest theoretical density (6.09 g/cm^3), which is a desired property in aerospace field.[8,9] However, when the temperature is higher than 1200 °C, the oxidation resistance of ZrB_2 is poor, for the products of B_2O_3 volatilize fast, leaving the porous and nonprotective ZrO_2 layer.[10–13] Great efforts have been made to improve the oxidation resistance of ZrB_2 at over 1200 °C.[3,14–17] The addition of SiC can significantly improve the oxidation resistance at elevated temperature.[15,18–21] The formed glassy borosilicate is more viscous and has lower evaporation pressure. Besides, it is a better barrier to oxygen diffusion than boria.[22,23] So the glassy borosilicate can provide more efficient protection than boria.

The oxidation mechanism of UHTCs is very complicated. Numerous investigators have performed a lot of experiments to observe and analyze the microstructure evolution and the oxidation products during oxidation of UHTCs and have a certain understanding on the oxidation mechanism.[24–35] Wang et al.[35] synthesized ZrC–SiC powders and investigated the oxidation behavior. At low temperature, ZrC quickly oxidizes to form a nonprotective ZrO_2 layer, while protective SiO_2 forms to improve the oxidation resistance at ~1000 °C. Zhao et al.[34] analyzed the microstructure and phase composition for ZrC–30 vol% SiC oxidation from low temperature to ultrahigh temperature. Li et al.[33] fabricated three-dimensional needled C_f/ZrC–SiC and studied the mechanical properties, microstructure and high-temperature properties. They concluded that the excellent high-temperature properties are due to the formation of $ZrSiO_4$ on the surface. Zhang et al.[31] investigated the structure evolution and oxidation behavior of ZrB_2–SiC in a wide temperature range. The SiC content significantly affects the structure evolution over 1800 °C while it has no apparent influence below 1600 °C. Brent Bargeron et al.[32] studied the oxidation behavior of hafnium carbide in the temperature range 1400–2060 °C. Three distinct layers are found in the cross section, and the interlayer oxide is the best barrier for oxygen diffusion in the three layers. Lately, theoretical progress of UHTCs oxidation has been achieved. Parthasarathy et al.[36,37] proposed several models to describe the oxidation progress. The model can calculate the weight gain and oxidation kinetics and the results are in reasonable agreement with the experimental data. However, the growth strain in the oxidation process is not considered. The growth strain accompanying the metal oxidation process has been known for a long time.[38–41] Several theories have been proposed to explain the mechanism of the origin of the growth strain.[42–45] The Clarke's model is the most adopted. A lot of researches

Contributing Editor: Yanchun Zhou
[a)]Address all correspondence to this author.
e-mail: sshen@mail.xjtu.edu.cn
DOI: 10.1557/jmr.2016.489

https://doi.org/10.1557/jmr.2016.489 Published online by Cambridge University Press

 © Materials Research Society 2017

are based on the Clarke's model.[46–51] Moreover, the stress induced by the oxidation process in return can affect the oxidation kinetics.[52–57] Recently, based on the Parthasarathy et al.'s model,[36] Zhou et al.[58] proposed a thermo-chemo-mechanical model for the oxidation of ZrB_2. Panicaud et al.[59] reported the stress evolution in the case of oxidation of Zr alloy. The oxidation product of ZrB_2–SiC is ZrO_2, which is the same as that of Zr alloy. So there exists stress in the oxidation of ZrB_2–SiC, too. The stress analysis in the oxidation process is very essential to predict the cracking and spalling of the oxide. However, there are few investigations focused on the chemomechanical coupling issue in the oxidation process of ZrB_2–SiC.

In this work, a chemomechanical model for the oxidation and stress evolution in ZrB_2–SiC is proposed. The oxidation process can induce the stress and in return the stress can affect the molecular oxygen diffusion and oxidation reaction rate. The model can describe the evolutions of the stress in the oxide layer and the unoxidized substrate, oxide layer thickness, weight gain, pore radius, and pore volume fraction. The calculated results are consistent with the experimental observations.

II. Chemomechanical model

A. Model framework

The morphology of the oxide scale, the oxidation products and phase present are derived from the literature studies.[2,15,24,29,31,60] The oxidation schematic is shown in Fig. 1. Since the oxidation behavior of ZrB_2–SiC is different in different temperature ranges, the oxidation temperature in the model is limited to 1200–1800 °C, which is the range of engineering interest. The substrate is ZrB_2 containing dispersive SiC particles. The oxidation products are disconnected ZrO_2 grains (in cross section) with a continuous porous region which is filled with glassy borosilicate. In the limited range of temperature in the work, the permeability of molecular oxygen through the ZrO_2 grains is very small compared with that through the porous channels filled with glassy borosilicate, so the molecular oxygen permeating through the ZrO_2 grains is neglected, as presented in Parthasarathy et al.'s work.[36] The oxygen in the environment first dissolves in the glassy borosilicate then permeates through the outer glassy layer and the porous channels to react with the ZrB_2 at the interface 2 (see Fig. 1). A portion of oxygen diffuses through the SiC-depleted region to react with SiC at the interface 1 (see Fig. 1). The amount of oxygen is assumed to be proportional to the volume fraction of SiC. The volume fraction of SiC in the substrate is f_s. The porosity within ZrO_2 region is f_p. The glassy borosilicate volume fraction f_g and the ZrO_2 volume fraction f_{ZrO_2} in the region (2–3) of Fig. 1 are expressed as

$$f_g = f_s + f_p(1 - f_s) \quad , \tag{1}$$

$$f_{ZrO_2} = (1 - f_p)(1 - f_s) = 1 - f_g \quad . \tag{2}$$

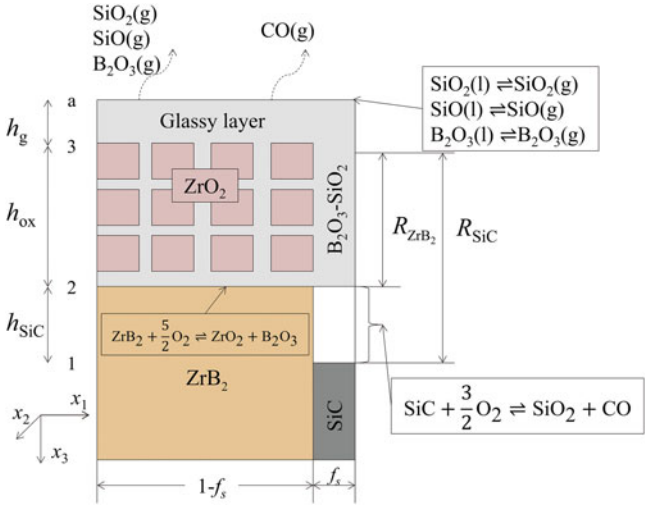


FIG. 1. Oxidation schematic of ZrB_2–SiC.

B. One-dimensional model

At the temperature range of 1200–1800 °C, the chemical reaction can be schematically expressed as

$$ZrB_2 + \frac{5}{2}O_2 = ZrO_2 + B_2O_3 \quad , \tag{3}$$

$$SiC + \frac{3}{2}O_2 = SiO_2 + CO \quad . \tag{4}$$

The thickness evolutions of the oxide and outer glassy layer are expressed as (details refer to Appendix)

$$\frac{dh_{ox}}{dt} = \frac{V_{ZrO_2}}{f_{ZrO_2}} k_1^0 \exp\left(\frac{\eta_p V_m \sigma_{kk}}{RT}\right)\left(C_{O_2}^{i2}\right)^{5/2} \quad , \tag{5}$$

$$\frac{dh_g}{dt} = \left[k_1^0 \exp\left(\frac{\eta_p V_m \sigma_{kk}}{RT}\right)\left(C_{O_2}^{i2}\right)^{5/2} - \left|J_{B_2O_3-vap}\right|\right] V_{B_2O_3} + \left[\frac{5}{3}\frac{f_s}{1-f_s} k_1^0 \exp\left(\frac{\eta_p V_m \sigma_{kk}}{RT}\right)\left(C_{O_2}^{i2}\right)^{5/2} - \left|J_{SiO_2-vap}\right| - \left|J_{SiO-vap}\right|\right] V_{SiO_2} - \frac{dh_{ox}}{dt} f_g \quad . \tag{6}$$

Equations (5) and (6) are Eqs. (A24) and (A25) in the Appendix. The variables in Eqs. (5) and (6) are defined in Appendix.

The recession rate of ZrB_2 and SiC is related to the change rate of h_{ox} through molar volume and volume fraction.

https://doi.org/10.1557/jmr.2016.489 Published online by Cambridge University Press

$$\frac{dR_{ZrB_2}}{dt} = \frac{V_{ZrB_2}}{V_{ZrO_2}} \frac{f_{ZrO_2}}{(1-f_s)} \frac{dh_{ox}}{dt} \quad , \tag{7}$$

$$\frac{dR_{SiC}}{dt} = \frac{5}{3} \frac{V_{SiC} f_{ZrO_2}}{V_{ZrO_2}(1-f_s)} \frac{dh_{ox}}{dt} \quad , \tag{8}$$

where V_{ZrB_2} and V_{SiC} are the molar volume of ZrB_2 and SiC, respectively. R_{ZrB_2} and R_{SiC} are the recession thickness of ZrB_2 and SiC, respectively.

Then the SiC-depleted layer thickness h_{SiC} is easily expressed as

$$h_{SiC} = R_{SiC} - R_{ZrB_2} \quad . \tag{9}$$

The weight gain due to the oxidation is expressed as

$$W_g = h_{ox}\left(f_{ZrO_2}\rho_{ZrO_2} + f_g\rho_g\right) + h_g\rho_g - R_{SiC}f_s\rho_{SiC} - R_{ZrB_2}(1-f_s)\rho_{ZrB_2} \quad , \tag{10}$$

where ρ_{ZrO_2}, ρ_{SiC}, ρ_{ZrB_2}, and ρ_g are the density of ZrO_2, SiC, ZrB_2, and borosilicate, respectively.

Accompanying the oxide layer growth, the stress is generated. The average stress in the oxide and substrate is expressed as follows (details refers to Appendix): Equations (11) and (12) are Eqs. (A48) and (A49) in the Appendix. The definition of variables in Eqs. (11) and (12) refers to Appendix.

$$\dot{\sigma}_{ox} = \left[B_{ox}\exp\left(-\frac{Q_{ox}}{RT}\right)(-\sigma_{ox})^{n_{ox}} + B_{sub}\exp\left(-\frac{Q_{sub}}{RT}\right)(-\sigma_{ox}h_{ox}/h_{sub})^{n_{sub}} + \left(\frac{1-v_{ox}}{E_{ox}^2}\dot{E}_{ox} - \frac{1-v_{sub}}{E_{sub}}\frac{\dot{h}_{ox}h_{sub} - h_{ox}\dot{h}_{sub}}{h_{sub}^2}\right)\sigma_{ox} - D_{ox}\dot{h}_{ox}\right] \Big/ \left(\frac{1-v_{ox}}{E_{ox}} + \frac{1-v_{sub}}{E_{sub}}h_{ox}\Big/h_{sub}\right) \quad , \tag{11}$$

$$\dot{\sigma}_{sub} = \left[B_{ox}\exp\left(-\frac{Q_{ox}}{RT}\right)(\sigma_{sub}h_{sub}/h_{ox})^{n_{ox}} + B_{sub}\exp\left(-\frac{Q_{sub}}{RT}\right)(\sigma_{sub})^{n_{sub}} + \left(\frac{1-v_{ox}}{E_{ox}}\frac{\dot{h}_{sub}h_{ox} - h_{sub}\dot{h}_{ox}}{h_{ox}^2} - \frac{1-v_{ox}}{E_{ox}^2}\dot{E}_{ox}h_{sub}\Big/h_{ox}\right)\sigma_{sub} - D_{ox}\dot{h}_{ox}\right] \Big/ \left(-\frac{1-v_{ox}}{E_{ox}}h_{sub}\Big/h_{ox} - \frac{1-v_{sub}}{E_{sub}}\right) \quad . \tag{12}$$

For the porous oxide layer, the relationship between Yong's modulus and porosity is[61]

$$E_{ox} = \frac{E_{ox}^0}{1 + \frac{4f_g(1-v_{ox}^2)}{\pi}} \quad , \tag{13}$$

where E_{ox}^0 is the Yong's modulus of oxide when there is no pore.

The variation of pore radius r and borosilicate volume fraction f_g is

$$r = r^0\left(1 + \varepsilon_{pore}\right) \quad , \tag{14}$$

$$f_g = f_g^0\left(1 + \varepsilon_{pore}\right)^2 \quad , \tag{15}$$

where r^0 and f_g^0 are the pore radius and glassy borosilicate volume fraction when there is no stress.

III. RESULTS AND DISCUSSIONS

The temperature is 1600 °C and the material properties used in the calculation are listed in Table I. Figure 2 shows the thickness calculated by the model and the experimental data. The total thickness (oxide + glass), the oxide thickness and the SiC-depleted region thickness are all plotted. The calculated total thickness and the oxide thickness are both in good agreement with the experimental data, which validates the proposed model. Since the SiC-depleted region is indistinct in experiment observation, the experimental data of SiC-depleted region thickness is not available. So the calculated SiC-depleted region thickness is not compared with the experimental data. The solid line represents the total thickness of the oxide and glassy layer. The dotted line represents the thickness of the oxide. It can be easily seen from Fig. 2 that the outer glassy layer is almost the same thickness as the oxide thickness. The outer glassy layer is a barrier for oxygen diffusion which can provide excellent protection. So the good oxidation resistance of

https://doi.org/10.1557/jmr.2016.489 Published online by Cambridge University Press

TABLE I. Material properties used in the calculation.

		ZrB_2–SiC	
	ZrO_2	15% SiC	20% SiC
Young's modulus (E/GPa)	115 (Ref. 62)	278 (Ref. 63)	283 (Ref. 63)
Poisson's ratio (ν)	0.33 (Ref. 64)	0.16 (Ref. 65)	0.16 (Ref. 65)
Norton stress exponent (n)	~1.3 (Ref. 66)	~1 (Ref. 67)	~1 (Ref. 67)
Material creep coefficient [B/(MPa^{-n}/s)]	1×10^5 (Ref. 66)	0.0455 (Ref. 67)	0.2537 (Ref. 67)
Activation energy [Q/(kJ/mol)]	517 (Ref. 66)	240 (Ref. 67)	258 (Ref. 67)

SiC-containing ZrB_2 is due to the formation of the relatively thick outer glassy layer.

The weight gain calculated by the proposed model is compared with the experimental data in Fig. 3. The weight gain is controlled not only by the formation of oxidation products but also by the evaporation of the liquid products. The calculated weight gain is almost parabolic and in reasonable agreement with the experimental data.

The stress evolution in the oxide layer is shown in Fig. 4. First, the compressive stress in the oxide layer increases with time, for the dominant factor is the growth strain. When the stress reaches the peak value, the stress begins to decrease with time, which is because the creep strain is dominant now. For different growth coefficient D_{ox}, the trend of stress in the oxide layer is the same but the value of the stress increases with increasing the

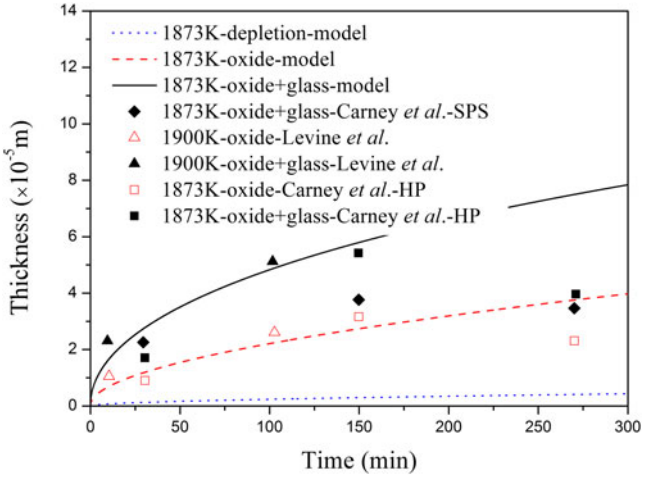


FIG. 2. Calculated oxide layer thickness compared with experimental data[2,60] for ZrB_2–20 vol% SiC oxidized at 1873 K [from Eqs. (5), (6), and (9)].

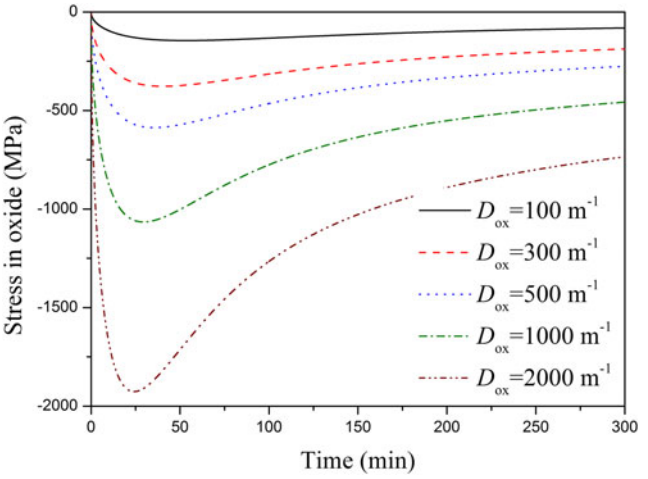


FIG. 4. Stress evolution in the oxide layer for ZrB_2–20 vol% SiC oxidized at 1873 K [from Eq. (11)].

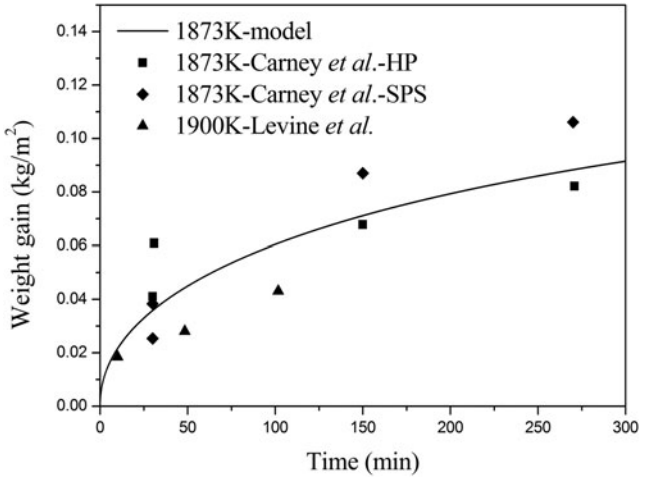


FIG. 3. Calculated weight gain compared with experimental data[2,60] for ZrB_2–20 vol% SiC oxidized at 1873 K [from Eq. (10)].

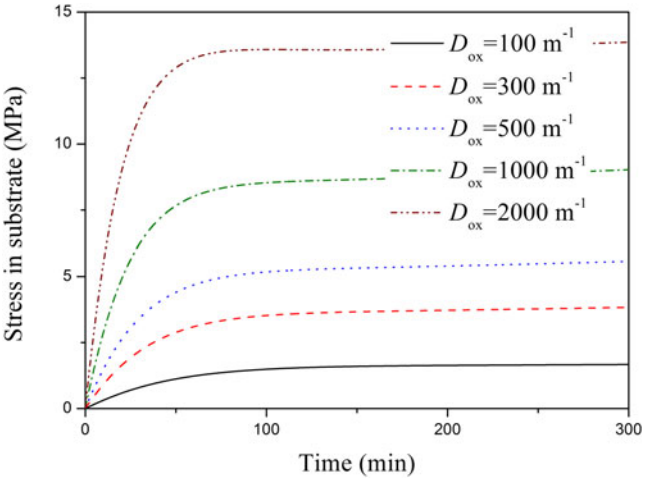


FIG. 5. Stress evolution in the substrate for ZrB_2–20 vol% SiC oxidized at 1873 K [from Eq. (12)].

https://doi.org/10.1557/jmr.2016.489 Published online by Cambridge University Press

growth coefficient. Figure 5 shows the stress evolution in the substrate. The stress in the substrate is tensile. The stress increases first, then the stress almost remains the same. This is because the stress is dominated by the growth strain in the oxide layer in short oxidation time. As the oxidation time is prolonged, the creep strain becomes remarkable. The stress release rate is almost equal to the stress increasing rate. The stress almost remains unchanged. For different growth coefficient, the stress variation has the similar trend but increases with increasing the growth coefficient.

Since the stress in the oxide layer can affect the pore radius and the borosilicate volume fraction, the pore radius and the borosilicate volume fraction varies with time too. Figures 6 and 7 show the pore radius evolution with time and the borosilicate volume fraction evolution with time, respectively. It can be seen that the pore radius shrinks with time. The larger the growth coefficient is, the more the pore radius shrinks. The reason is that the compressive stress increases with the growth coefficient and the larger the compressive stress is, the more the pore radius shrinks. The borosilicate volume fraction has the same trend as the pore radius, for both of them are the characterizations of the effect of stress on the pore.

Figures 8 and 9 show the effect of different volume fraction additions of SiC on the ZrB_2–SiC oxidation behavior. It is obvious that the ZrB_2 with 20% volume fraction addition of SiC has thinner oxide layer thickness and smaller weight gain than that with 15% volume fraction addition of SiC. The addition of SiC particles can significantly reinforce the oxidation resistance of ZrB_2 at elevated temperature. This is because the products of glassy SiO_2 have very small evaporation pressure. Besides, the diffusivity of oxygen in glassy SiO_2 is

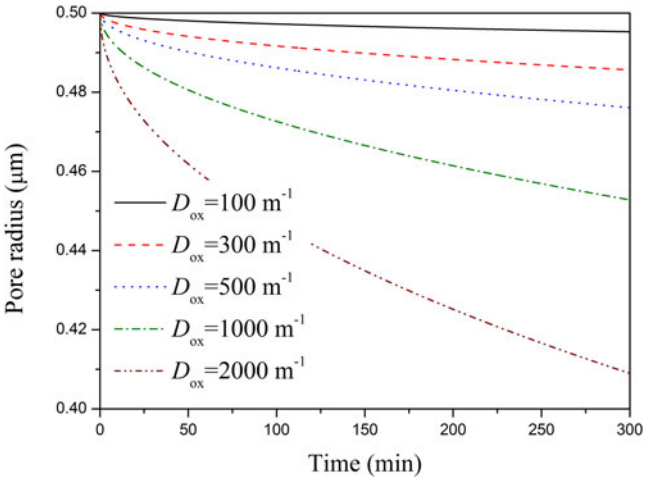


FIG. 6. Pore radius evolution for ZrB_2–20 vol% SiC oxidized at 1873 K [from Eq. (14)].

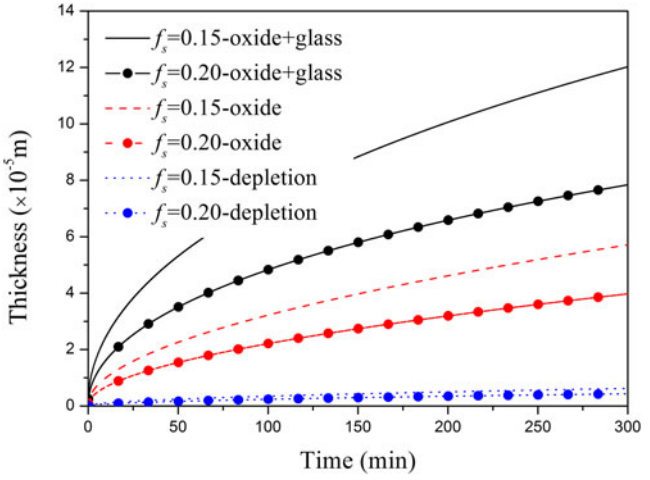


FIG. 8. Oxide layer thickness for ZrB_2 with different SiC content oxidized at 1873 K [from Eqs. (5), (6) and (9)].

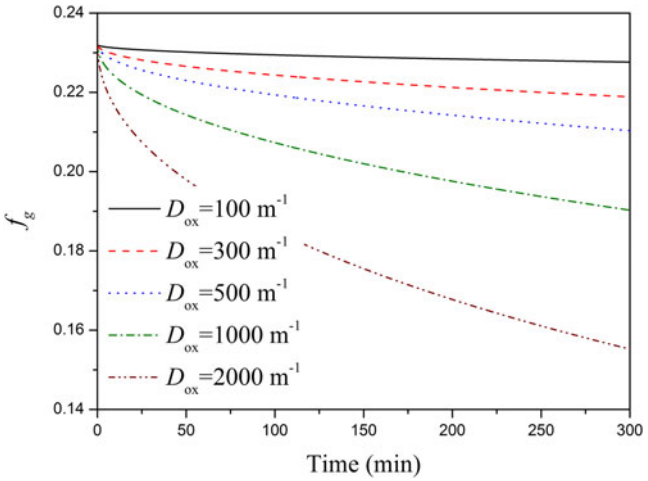


FIG. 7. fg evolution for ZrB_2–20 vol% SiC oxidized at 1873 K [from Eq. (15)].

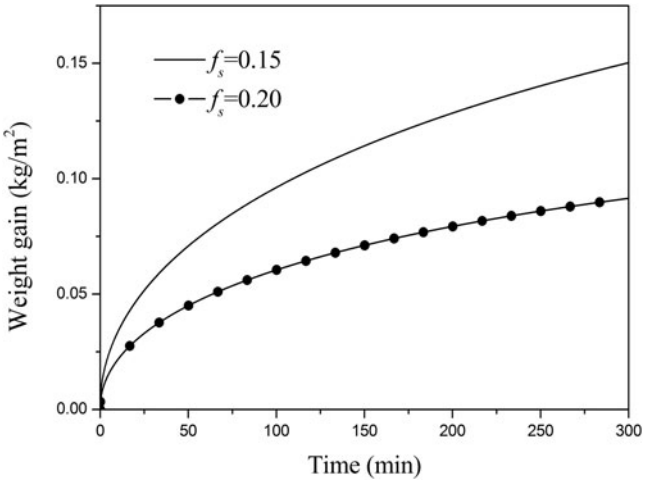


FIG. 9. Weight gain for ZrB_2 with different SiC contents oxidized at 1873 K [from Eq. (10)].

https://doi.org/10.1557/jmr.2016.489 Published online by Cambridge University Press

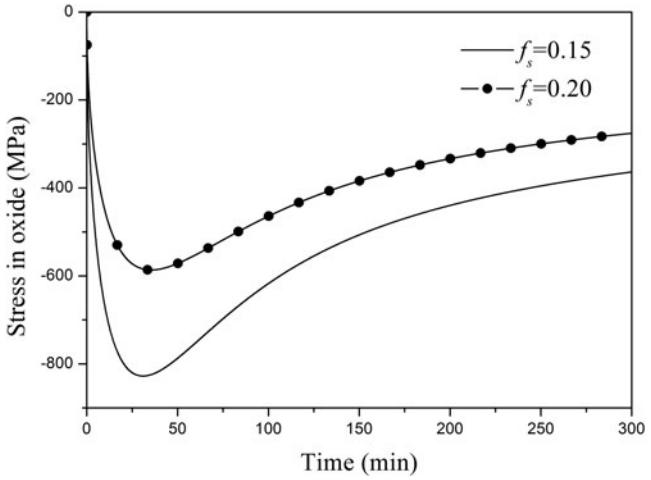


FIG. 10. Stress evolution in the oxide layer for ZrB_2 with different SiC content oxidized at 1873 K [from Eq. (11)].

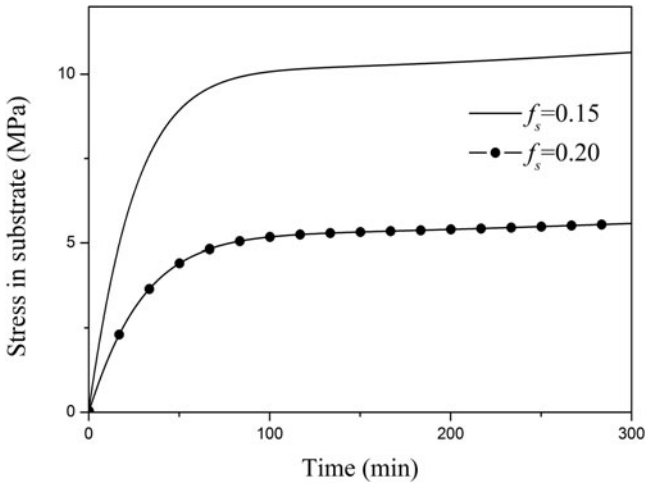


FIG. 11. Stress evolution in the substrate for ZrB_2 with different SiC content oxidized at 1873 K [from Eq. (12)].

much smaller than that in glassy B_2O_3. The formed outer glassy borosilicate of ZrB_2 with higher volume fraction addition of SiC contains more SiO_2 than that with lower volume fraction addition of SiC. So the ZrB_2 with higher volume fraction addition of SiC has more excellent oxidation resistance. The oxidation rate is slower, which results in thinner oxide layer thickness and smaller weight gain.

Since the ZrB_2 with 20% volume fraction addition of SiC has thinner oxide layer, it is obvious that the stress should also be smaller. It can be seen from Figs. 10 and 11 that both the stresses in the oxide layer and the substrate are smaller for 20% volume fraction addition of SiC.

IV. CONCLUSIONS

A chemomechanical model is proposed for the oxidation and stress evolution in ZrB_2–SiC. The model focuses on the coupling effects of chemical reaction and mechanics. The stress state in the oxidation process is very essential to predict the cracking and spalling of the oxide. Accompanying the oxidation process, the stress generates. The stress induced by the oxidation can affect the oxidation reaction rate and the oxygen diffusion. The volume fraction of SiC has great influence on the oxidation process. Due to that SiO_2 has excellent barrier for oxygen diffusion and low evaporation pressure, the ZrB_2 with higher volume fraction addition of SiC has thinner oxide layer thickness, lower weight gain and smaller stress. The calculated results are consistent with experimental data.

ACKNOWLEDGMENTS

This work is supported by the National Natural Science Foundation of China (NSFC Grants No. 11632014, 11372238, 11302161 and 11302162) and the Chang Jiang Scholar program.

REFERENCES

1. K. Upadhya, J-M. Yang, and W.P. Hoffman: Materials for ultrahigh temperature structural applications. *Am. Ceram. Soc. Bull.* **76**(12), 51 (1997).
2. S.R. Levine, E.J. Opila, M.C. Halbig, J.D. Kiser, M. Singh, and J.A. Salem: Evaluation of ultra-high temperature ceramics for aeropropulsion use. *J. Eur. Ceram. Soc.* **22**(14), 2757 (2002).
3. A. Chamberlain, W. Fahrenholtz, G. Hilmas, and D. Ellerby: Oxidation of ZrB_2–SiC ceramics under atmospheric and reentry conditions. *Refract. Appl. Trans.* **1**(2), 1 (2005).
4. F. Monteverde: The thermal stability in air of hot-pressed diboride matrix composites for uses at ultra-high temperatures. *Corros. Sci.* **47**(8), 2020 (2005).
5. R. Savino, M.D.S. Fumo, D. Paterna, and M. Serpico: Aero-thermodynamic study of UHTC-based thermal protection systems. *Aerosp. Sci. Technol.* **9**(2), 151 (2005).
6. R. Monti, M.D. Stefano Fumo, and R. Savino: Thermal shielding of a reentry vehicle by ultra-high-tempreature ceramic materials. *J. Thermophys. Heat Transfer* **20**(3), 500 (2006).
7. F. Monteverde and L. Scatteia: Resistance to thermal shock and to oxidation of metal diborides-SiC ceramics for aerospace application. *J. Am. Ceram. Soc.* **90**(4), 1130 (2007).
8. W.G. Fahrenholtz, G.E. Hilmas, I.G. Talmy, and J.A. Zaykoski: Refractory diborides of zirconium and hafnium. *J. Am. Ceram. Soc.* **90**(5), 1347 (2007).
9. R. Tandon, H.P. Dumm, E.L. Corral, R.E. Loehman, and P.G. Kotula: Ultra high temperature ceramics for hypersonic vehicle applications. In *Technical Report No. SAND 2006-2925* (Sandia National Laboratories, Albuquerque, New Mexico, USA, 2006).
10. W. Tripp and H. Graham: Thermogravimetric study of the oxidation of ZrB_2 in the temperature range of 800° to 1500 °C. *J. Electrochem. Soc.* **118**(7), 1195 (1971).
11. W.G. Fahrenholtz: The ZrB_2 volatility diagram. *J. Am. Ceram. Soc.* **88**(12), 3509 (2005).
12. A.K. Kuriakose and J. Margrave: The oxidation kinetics of zirconium diboride and zirconium carbide at high temperatures. *J. Electrochem. Soc.* **111**(7), 827 (1964).

https://doi.org/10.1557/jmr.2016.489 Published online by Cambridge University Press

13. J.B. Berkowitz-Mattuck: High-temperature oxidation III. Zirconium and hafnium diborides. *J. Electrochem. Soc.* **113**(9), 908 (1966).
14. W. Tripp, H. Davis, and H. Graham: Effect of an SiC addition on the oxidation of ZrB_2. *Am. Ceram. Soc. Bull.* **52**(8), 612 (1973).
15. F. Monteverde and A. Bellosi: Oxidation of ZrB_2-based ceramics in dry air. *J. Electrochem. Soc.* **150**(11), B552 (2003).
16. P. Hu, W. Guolin, and Z. Wang: Oxidation mechanism and resistance of ZrB_2–SiC composites. *Corros. Sci.* **51**(11), 2724 (2009).
17. W.B. Han, P. Hu, X.H. Zhang, J.C. Han, and S.H. Meng: High-temperature oxidation at 1900 °C of ZrB_2–*x*SiC ultrahigh-temperature ceramic composites. *J. Am. Ceram. Soc.* **91**(10), 3328 (2008).
18. F. Monteverde and A. Bellosi: Development and characterization of metal-diboride-based composites toughened with ultra-fine SiC particulates. *Solid State Sci.* **7**(5), 622 (2005).
19. S.S. Hwang, A.L. Vasiliev, and N.P. Padture: Improved processing and oxidation-resistance of ZrB_2 ultra-high temperature ceramics containing SiC nanodispersoids. *Mater. Sci. Eng., A* **464**(1), 216 (2007).
20. F. Monteverde: Beneficial effects of an ultra-fine α-SiC incorporation on the sinterability and mechanical properties of ZrB_2. *Appl. Phys. A* **82**(2), 329 (2006).
21. S. Zhu, W.G. Fahrenholtz, and G.E. Hilmas: Influence of silicon carbide particle size on the microstructure and mechanical properties of zirconium diboride–silicon carbide ceramics. *J. Eur. Ceram. Soc.* **27**(4), 2077 (2006).
22. S.N. Karlsdottir, J.W. Halloran, and C.E. Henderson: Convection patterns in liquid oxide films on ZrB_2–SiC composites oxidized at a high temperature. *J. Am. Ceram. Soc.* **90**(9), 2863 (2007).
23. S.N. Karlsdottir and J.W. Halloran: formation of oxide scales on zirconium diboride–silicon carbide composites during oxidation: Relation of subscale recession to liquid oxide flow. *J. Am. Ceram. Soc.* **91**(11), 3652 (2008).
24. A. Rezaie, W.G. Fahrenholtz, and G.E. Hilmas: Evolution of structure during the oxidation of zirconium diboride–silicon carbide in air up to 1500 °C. *J. Eur. Ceram. Soc.* **27**(6), 2495 (2007).
25. J. Han, P. Hu, X. Zhang, and S. Meng: Oxidation behavior of zirconium diboride–silicon carbide at 1800 °C. *Scr. Mater.* **57**(9), 825 (2007).
26. C. Tian, D. Gao, Y. Zhang, C. Xu, Y. Song, and X. Shi: Oxidation behaviour of zirconium diboride–silicon carbide ceramic composites under low oxygen partial pressure. *Corros. Sci.* **53**(11), 3742 (2011).
27. A. Rezaie, W.G. Fahrenholtz, and G.E. Hilmas: Oxidation of zirconium diboride–silicon carbide at 1500 °C at a low partial pressure of oxygen. *J. Am. Ceram. Soc.* **89**(10), 3240 (2006).
28. P.A. Williams, R. Sakidja, J.H. Perepezko, and P. Ritt: Oxidation of ZrB_2–SiC ultra-high temperature composites over a wide range of SiC content. *J. Eur. Ceram. Soc.* **32**(14), 3875 (2012).
29. E.J. Opila and M.C. Halbig: Oxidation of ZrB_2–SiC. *Ceram. Eng. Sci. Proc.* **22**(3), 221 (2001).
30. J. Han, P. Hu, X. Zhang, S. Meng, and W. Han: Oxidation-resistant ZrB_2–SiC composites at 2200 °C. *Compos. Sci. Technol.* **68**(3), 799 (2008).
31. X-H. Zhang, P. Hu, and J-C. Han: Structure evolution of ZrB_2–SiC during the oxidation in air. *J. Mater. Res.* **23**(7), 1961 (2008).
32. C.B. Bargeron, R.C. Benson, A.N. Jette, and T.E. Phillips: Oxidation of hafnium carbide in the temperature range 1400° to 2060 °C. *J. Am. Ceram. Soc.* **76**(4), 1040 (1993).
33. Q. Li, S. Dong, Z. Wang, P. He, H. Zhou, J. Yang, B. Wu, and J. Hu: Fabrication and properties of 3-D C_f/SiC-ZrC composites, using ZrC precursor and polycarbosilane. *J. Am. Ceram. Soc.* **95**(4), 1216 (2012).
34. L. Zhao, D. Jia, X. Duan, Z. Yang, and Y. Zhou: Oxidation of ZrC–30 vol% SiC composite in air from low to ultrahigh temperature. *J. Eur. Ceram. Soc.* **32**(4), 947 (2012).
35. X.F. Wang, J.C. Liu, F. Hou, J.D. Hu, X. Sun, and Y-C. Zhou: Synthesis of ZrC–SiC powders from hybrid liquid precursors with improved oxidation resistance. *J. Am. Ceram. Soc.* **98**(1), 197 (2015).
36. T. Parthasarathy, R. Rapp, M. Opeka, and R. Kerans: A model for the oxidation of ZrB_2, HfB_2 and TiB_2. *Acta Mater.* **55**(17), 5999 (2007).
37. T. Parthasarathy, R. Rapp, M. Opeka, and M. Cinibulk: Modeling oxidation kinetics of SiC-containing refractory diborides. *J. Am. Ceram. Soc.* **95**(1), 338 (2012).
38. U. Evans: The mechanism of oxidation and tarnishing. *Trans. Electrochem. Soc.* **91**(1), 547 (1947).
39. J. Stringer: Stress generation and relief in growing oxide films. *Corros. Sci.* **10**(7), 513 (1970).
40. V. Tolpygo and D. Clarke: Competition between stress generation and relaxation during oxidation of an Fe–Cr–Al–Y alloy. *Oxid. Met.* **49**(1–2), 187 (1998).
41. M. Schütze: *Protective Oxide Scales and Their Breakdown* (Wiley, Chichester, 1997).
42. R. Bedworth and N. Pilling: The oxidation of metals at high temperatures. *J. Inst. Met.* **29**(3), 529 (1923).
43. F. Rhines and J. Wolf: The role of oxide microstructure and growth stresses in the high-temperature scaling of nickel. *Metall. Trans.* **1**(6), 1701 (1970).
44. D.R. Clarke: The lateral growth strain accompanying the formation of a thermally grown oxide. *Acta Mater.* **51**(5), 1393 (2003).
45. B. Panicaud, J. Grosseau-Poussard, and J. Dinhut: General approach on the growth strain versus viscoplastic relaxation during oxidation of metals. *Comput. Mater. Sci.* **42**(2), 286 (2008).
46. Y. Zhang, X. Zhang, S-T. Tu, and F. Xuan: Analytical modeling on stress assisted oxidation and its effect on creep response of metals. *Oxid. Met.* **82**(3–4), 311 (2014).
47. S. Maharjan, X. Zhang, F. Xuan, Z. Wang, and S. Tu: Residual stresses within oxide layers due to lateral growth strain and creep strain: Analytical modeling. *J. Appl. Phys.* **110**(6), 063511 (2011).
48. X. Dong, X. Feng, and K-C. Hwang: Oxidation stress evolution and relaxation of oxide film/metal substrate system. *J. Appl. Phys.* **112**(2), 023502 (2012).
49. J-L. Grosseau-Poussard, B. Panicaud, and S. Ben Afia: Modelling of stresses evolution in growing thermal oxides on metals. A methodology to identify the corresponding mechanical parameters. *Comput. Mater. Sci.* **71**, 47 (2013).
50. B. Panicaud, J. Grosseau-Poussard, and J. Dinhut: On the growth strain origin and stress evolution prediction during oxidation of metals. *Appl. Surf. Sci.* **252**(16), 5700 (2006).
51. S. Maharjan, X. Zhang, and Z. Wang: Effect of oxide growth strain in residual stresses for the deflection test of single surface oxidation of alloys. *Oxid. Met.* **77**(1–2), 93 (2012).
52. R. Krishnamurthy and D.J. Srolovitz: Stress distributions in growing oxide films. *Acta Mater.* **51**(8), 2171 (2003).
53. R. Krishnamurthy and D.J. Srolovitz: Stress distributions in growing polycrystalline oxide films. *Acta Mater.* **52**(13), 3761 (2004).
54. H. Zhou, J. Qu, and M. Cherkaoui: Stress–oxidation interaction in selective oxidation of Cr–Fe alloys. *Mech. Mater.* **42**(1), 63 (2010).
55. X. Dong, X. Fang, X. Feng, and K.C. Hwang: Diffusion and stress coupling effect during oxidation at high temperature. *J. Am. Ceram. Soc.* **96**(1), 44 (2013).
56. H. Wang, Y. Suo, and S. Shen: Reaction–diffusion–stress coupling effect in inelastic oxide scale during oxidation. *Oxid. Met.* **83**(5–6), 507 (2015).

https://doi.org/10.1557/jmr.2016.489 Published online by Cambridge University Press

57. H. Wang and S. Shen: A chemomechanical model for stress evolution and distribution in the viscoplastic oxide scale during oxidation. *J. Appl. Mech.* **83**(5), 051008 (2016).
58. Z. Zhou, X. Peng, and Z. Wei: A thermo-chemo-mechanical model for the oxidation of zirconium diboride. *J. Am. Ceram. Soc.* **98**(2), 629 (2015).
59. B. Panicaud, J-L. Grosseau-Poussard, D. Retraint, M. Guérain, and L. Li: On the mechanical effects of a nanocrystallisation treatment for ZrO_2 oxide films growing on a zirconium alloy. *Corros. Sci.* **68**, 263 (2013).
60. C.M. Carney, P. Mogilvesky, and T.A. Parthasarathy: Oxidation behavior of zirconium diboride silicon carbide produced by the spark plasma sintering method. *J. Am. Ceram. Soc.* **92**(9), 2046 (2009).
61. W. Li, D. Li, C. Zhang, and D. Fang: Modelling the effect of temperature and damage on the fracture strength of ultra-high temperature ceramics. *Int. J. Fract.* **176**(2), 181 (2012).
62. E.Y. Fogaing, M. Huger, and C. Gault: Elastic properties and microstructure: Study of two fused cast refractory materials. *J. Eur. Ceram. Soc.* **27**(2), 1843 (2007).
63. M. Lugovy, V. Slyunyayev, N. Orlovskaya, E. Mitrentsis, C. Aneziris, T. Graule, and J. Kuebler: Temperature dependence of elastic properties of ZrB_2–SiC composites. *Ceram. Int.* **42**(2), 2439 (2016).
64. N. Noda: Thermal stresses intensity factor for functionally gradient plate with an edge crack. *J. Therm. Stresses.* **20**(3–4), 373 (1997).
65. J.W. Zimmermann, G.E. Hilmas, and W.G. Fahrenholtz: Thermal shock resistance of ZrB_2 and ZrB_2–30% SiC. *Mater. Chem. Phys.* **112**(1), 140 (2008).
66. J.D. French, J. Zhao, M.P. Harmer, H.M. Chan, and G.A. Miller: Creep of duplex microstructures. *J. Am. Ceram. Soc.* **77**(11), 2857 (1994).
67. I. Talmy, J. Zaykoski, and C. Martin: Flexural creep deformation of ZrB_2/SiC ceramics in oxidizing atmosphere. *J. Am. Ceram. Soc.* **91**(5), 1441 (2008).
68. S. Hu and S. Shen: Non-equilibrium thermodynamics and variational principles for fully coupled thermal–mechanical–chemical processes. *Acta Mech.* **224**(12), 2895 (2013).
69. J. Li: Chemical potential for diffusion in a stressed solid. *Scr. Metall.* **15**(1), 21 (1981).
70. N. Swaminathan, J. Qu, and Y. Sun: An electrochemomechanical theory of defects in ionic solids. I. Theory. *Philos. Mag.* **87**(11), 1705 (2007).
71. Y. Suo and S. Shen: General approach on chemistry and stress coupling effects during oxidation. *J. Appl. Phys.* **114**(16), 164905 (2013).
72. O. Golan, A. Arbel, D. Eliezer, and D. Moreno: The applicability of Norton's creep power law and its modified version to a single-crystal superalloy type CMSX-2. *Mater. Sci. Eng., A* **216**(1), 125 (1996).
73. L. Dormieux, D. Kondo, and F-J. Ulm: *Microporomechanics* (John Wiley & Sons, Chichester, U.K., 2006).

APPENDIX: FORMULATION OF THE CHEMOMECHANICAL MODEL

1. Chemical Gibbs function variation

For the fully coupled chemomechanical process, the following chemical Gibbs function variation is obtained:[68]

$$\delta\Pi_{gc} = \int_V \delta g_c \, dV + \delta D_{gc} - \delta Q^* - \delta W^* = 0 \quad , \quad \text{(A1)}$$

where g_c is the chemical Gibbs function, and D_{gc} is the complement dissipative energy. Q^* and W^* are the complement heart absorbed from the external heart source and work of the external mechanical force. In the case of ZrB_2–SiC oxidation at high temperature, the oxidation reaction occurs at the interface between the oxide and substrate. By the same derivational process in Ref. 68, one gets

$$\begin{aligned}\delta\Pi_{gc} = 0 = &\int_a \left(\sigma_{ij}n_j - T_i^*\right)\delta u_i \, da \\ &- \int_V \left(\sigma_{ij,j} + f_i - \rho\ddot{u}_i\right)\delta u_i \, dV - \int_\Gamma \left\|\sigma_{ij}n_j\right\|\delta u_i \, d\Gamma \\ &- \int_0^t \int_V \left(\dot{c}_N + c_N v_{k,k} + J_{i,i}^N\right)\delta\mu_N \, dV \, d\tau \\ &+ \int_0^t \int_a \left(J_i^N n_i - J_N^*\right)\delta\mu_N da \, d\tau \\ &- \int_0^t \int_\Gamma \left\{\left\|c_N(v_k - V_k)\right\|n_k + \left\|J_i^N n_i\right\| \right. \\ &\left. - v_{Nr}\dot{w}_r\right\}\delta\mu_N \, d\Gamma \, d\tau \quad , \end{aligned} \quad \text{(A2)}$$

where σ_{ij}, T_i^*, u_i, f_i, and ρ are the stress, surface traction, displacement, body force, and density, respectively. v_k is the particle velocity. c_N, J_i^N, and μ_N are the molar fraction, diffusion flux, and chemical potential of species N, respectively. v_{Nr} and $\dot{w}_r$ are the stoichiometric coefficient and reaction rate of the rth reaction, respectively. J_N^* is the diffusion flux of species N on the boundary. V_k is the velocity of the moving interface Γ. n_i is the component of the normal vector of the boundary and interface. $\|\cdot\|$ denotes the jump.

Due to the arbitrariness of δu_i and $\delta\mu_N$, one can get from Eq. (A2) the governing equations

$$\sigma_{ij,j} + f_i = \rho\ddot{u}_i \quad \text{(A3)}$$

$$\dot{c}_N = -c_N v_{k,k} - J_{i,i}^N \quad \text{(A4)}$$

and the boundary conditions

$$\begin{aligned}\sigma_{ij}n_j &= T_i^* \quad \text{on } a_\sigma \\ J_i^N n_i &= J_N^* \quad \text{on } a_{dn} \quad . \end{aligned} \quad \text{(A5)}$$

On the moving interface, one can get the jump conditions

$$\begin{aligned}&\left\|\sigma_{ij}n_j\right\| = 0 \quad , \\ &\left\|c_N(v_k - V_k)\right\|n_k + \left\|J_i^N n_i\right\| - v_{Nr}\dot{w}_r = 0 \quad . \end{aligned} \quad \text{(A6)}$$

2. One-dimensional model

At the temperature range of 1200–1800 °C, the chemical reaction can be schematically expressed as

https://doi.org/10.1557/jmr.2016.489 Published online by Cambridge University Press

$$ZrB_2 + \frac{5}{2}O_2 = ZrO_2 + B_2O_3 \quad , \tag{A7}$$

$$SiC + \frac{3}{2}O_2 = SiO_2 + CO \quad . \tag{A8}$$

According to the law of mass action, the chemical reaction rate of Eq. (A7) is[52,54]

$$\dot{w}_1 = k_1\left(C_{O_2}^{i2}\right)^{5/2} \quad , \tag{A9}$$

where k_1 is the chemical reaction rate constant of Eq. (A7). $C_{O_2}^{i2}$ is the molar concentration of oxygen at the interface 2 in Fig. 1. The molar fraction and molar concentration are related by $c_{O_2} = V_m C_{O_2}$, where V_m is the average molar volume of the oxide per atom.

Based on the assumption that the amount of oxygen consumed by the SiC is proportional to the volume fraction of SiC, the following expression is obtained.

$$\dot{w}_2 = \frac{5}{3}\frac{f_s}{1-f_s}k_1\left(C_{O_2}^{i2}\right)^{5/2} \quad , \tag{A10}$$

where $\dot{w}_2$ is the chemical reaction rate of Eq. (A8).

The generated ZrO_2 causes the growth of the oxide layer. According to the conservation of zirconium atom, one can get

$$\frac{dh_{ox}}{dt} = \frac{V_{ZrO_2}}{f_{ZrO_2}}\dot{w}_1 \quad , \tag{A11}$$

where h_{ox} and V_{ZrO_2} are the thickness of the oxide layer and molar volume of the ZrO_2, respectively.

The net increase of liquid products (SiO_2 and B_2O_3) first fills up the pore in the oxide layer, then forms the outer glassy layer. The outer glassy layer thickness h_g is expressed as

$$\frac{dh_g}{dt} = \left(\dot{w}_1 - \left|J_{B_2O_3-vap}\right|\right)V_{B_2O_3} + \left(\dot{w}_2 - \left|J_{SiO_2-vap}\right| - \left|J_{SiO-vap}\right|\right)V_{SiO_2} - \frac{dh_{ox}}{dt}f_g \quad , \tag{A12}$$

where $J_{B_2O_3-vap}$, J_{SiO_2-vap}, and $J_{SiO-vap}$ are the evaporation flux of B_2O_3, SiO_2, and SiO at the surface, respectively. $V_{B_2O_3}$ and V_{SiO_2} are the molar volume of B_2O_3 and SiO_2, respectively.

The recession rate of ZrB_2 and SiC is related to the change rate of h_{ox} through molar volume and volume fraction.

$$\frac{dR_{ZrB_2}}{dt} = \frac{V_{ZrB_2}}{V_{ZrO_2}}\frac{f_{ZrO_2}}{(1-f_s)}\frac{dh_{ox}}{dt} \quad , \tag{A13}$$

$$\frac{dR_{SiC}}{dt} = \frac{5}{3}\frac{V_{SiC}f_{ZrO_2}}{V_{ZrO_2}(1-f_s)}\frac{dh_{ox}}{dt} \quad , \tag{A14}$$

where V_{ZrB_2} and V_{SiC} are the molar volume of ZrB_2 and SiC, respectively. R_{ZrB_2} and R_{SiC} are the recession thickness of ZrB_2 and SiC, respectively.

Then the SiC-depleted layer thickness h_{SiC} is easily expressed as

$$h_{SiC} = R_{SiC} - R_{ZrB_2} \quad . \tag{A15}$$

The weight gain due to the oxidation is expressed as

$$W_g = h_{ox}\left(f_{ZrO_2}\rho_{ZrO_2} + f_g\rho_g\right) + h_g\rho_g - R_{SiC}f_s\rho_{SiC} - R_{ZrB_2}(1-f_s)\rho_{ZrB_2} \quad , \tag{A16}$$

where ρ_{ZrO_2}, ρ_{SiC}, ρ_{ZrB_2}, and ρ_g are the density of ZrO_2, SiC, ZrB_2, and borosilicate, respectively.

Ignoring the convection item, Eq. (A4) is written as

$$\frac{\partial C_{O_2}}{\partial t} = -\frac{\partial J_3^{O_2}}{\partial x_3} \quad , \tag{A17}$$

where $J_3^{O_2}$ is the flux of oxygen in x_3 direction.

The stress-dependent chemical potential of oxygen is[69]

$$\mu_{O_2} = \mu_{O_2}^0 + RT\ln(V_m C_{O_2}) - \eta_{O_2}V_m\sigma_{kk} \quad , \tag{A18}$$

where R and T are the gas constant and absolute temperature, respectively. η_{O_2} and σ_{kk} are the coefficient of compositional expansion and hydrostatic stress in the oxide layer. $\mu_{O_2}^0$ is the chemical potential at the reference state.

The oxygen flux is expressed as

$$J_3^{O_2} = -\frac{D_{O_2-g}C_{O_2}}{RT}\frac{\partial \mu_{O_2}}{\partial x_3} = -D_{O_2-g}\left(\frac{\partial C_{O_2}}{\partial x_3} - \frac{\eta_{O_2}V_m}{RT}C_{O_2}\frac{\partial \sigma_{kk}}{\partial x_3}\right) \quad , \tag{A19}$$

where D_{O_2-g} is the diffusivity of oxygen in the glassy borosilicate.

Then, Eq. (A17) can be rewritten as

$$\frac{\partial C_{O_2}}{\partial t} = -\frac{\partial J_3^{O_2}}{\partial x_3} = D_{O_2-g}\left(\frac{\partial^2 C_{O_2}}{\partial^2 x_3} - \frac{\eta_{O_2}V_m}{RT}\frac{\partial C_{O_2}}{\partial x_3}\frac{\partial \sigma_{kk}}{\partial x_3} - \frac{\eta_{O_2}V_m C_{O_2}}{RT}\frac{\partial^2 \sigma_{kk}}{\partial^2 x_3}\right) \quad . \tag{A20}$$

https://doi.org/10.1557/jmr.2016.489 Published online by Cambridge University Press

Since the chemical potential is stress-dependent, the chemical reaction is stress-dependent too. The stress-dependent chemical reaction rate constant is expressed as[54,70]

$$k_1 = k_1^0 \exp\left(\frac{\eta_p V_m \sigma_{kk}}{RT}\right) \quad , \tag{A21}$$

where p represents the oxide. k_1^0 is the chemical reaction rate constant when there is no stress.

Stress-dependent chemical reaction rate is

$$\dot{w}_1 = k_1^0 \exp\left(\frac{\eta_p V_m \sigma_{kk}}{RT}\right)\left(C_{O_2}^{i2}\right)^{5/2} \quad , \tag{A22}$$

$$\dot{w}_2 = \frac{5}{3}\frac{f_s}{1-f_s} k_1^0 \exp\left(\frac{\eta_p V_m \sigma_{kk}}{RT}\right)\left(C_{O_2}^{i2}\right)^{5/2} \quad . \tag{A23}$$

Substituting Eqs. (A22) and (A23) into Eqs. (A11) and (A12), they are rewritten as

$$\frac{dh_{ox}}{dt} = \frac{V_{ZrO_2}}{f_{ZrO_2}} k_1^0 \exp\left(\frac{\eta_p V_m \sigma_{kk}}{RT}\right)\left(C_{O_2}^{i2}\right)^{5/2} \quad , \tag{A24}$$

$$\begin{aligned}\frac{dh_g}{dt} = &\left[k_1^0 \exp\left(\frac{\eta_p V_m \sigma_{kk}}{RT}\right)\left(C_{O_2}^{i2}\right)^{5/2} - \left|J_{B_2O_3-vap}\right|\right] V_{B_2O_3} \\ &+ \left[\frac{5}{3}\frac{f_s}{1-f_s} k_1^0 \exp\left(\frac{\eta_p V_m \sigma_{kk}}{RT}\right)\left(C_{O_2}^{i2}\right)^{5/2}\right. \\ &\left. - \left|J_{SiO_2-vap}\right| - \left|J_{SiO-vap}\right|\right] V_{SiO_2} - \frac{dh_{ox}}{dt} f_g \quad . \end{aligned} \tag{A25}$$

The evaporation flux at the surface is express as follows

$$\left|J_{species-vap}\right| = \frac{D_{species}}{RT} 10^5 \frac{p_{species-vap}}{\delta_{bdry}};$$

$$\delta_{bdry} = \frac{3}{2}\sqrt{\frac{l_{specimen}}{v_{fluid}}}\left(\frac{\eta_{fluid}}{\rho_{fluid}}\right)^{1/6}\left(D_{species}\right)^{1/3} \quad , \tag{A26}$$

where $D_{species}$ is the diffusivity in mixed gas. $p_{species-vap}$ is the evaporation pressure. Species refers to SiO_2, B_2O_3, and SiO. δ_{bdry} is the boundary layer thickness. $l_{specimen}$ is the length of the specimen. v_{fluid}, η_{fluid}, and ρ_{fluid} are the velocity, viscosity, and density of the ambient fluid, respectively.

According to Eq. (A6), the moving boundary condition of the interface 2 is

$$\begin{aligned} J_3^{O_2,i2} &= f_g C_{O_2}^{i2} V + \frac{5}{2}\dot{w}_1 + \frac{3}{2}\dot{w}_2 \\ &= f_g C_{O_2}^{i2} \frac{V_{ZrO_2}}{f_{ZrO_2}} k_1^0 \exp\left(\frac{\eta_p V_m \sigma_{kk}}{RT}\right)\left(C_{O_2}^{i2}\right)^{5/2} \\ &\quad + \frac{1}{1-f_s}\frac{5}{2} k_1^0 \exp\left(\frac{\eta_p V_m \sigma_{kk}}{RT}\right)\left(C_{O_2}^{i2}\right)^{5/2} \quad , \end{aligned} \tag{A27}$$

where $J_3^{O_2,i2}$ is the oxygen flux at the interface 2. V is the velocity of the interface 2 and is expressed as

$$V = \frac{dh_{ox}}{dt} \quad . \tag{A28}$$

At the interface 3, the flux of the oxygen is equal.

$$J_3^{O_2,i3+} = J_3^{O_2,i3-} \tag{A29}$$

Since the quasi-steady state is assumed, the oxygen flux can be expressed as

$$J_3^{O_2,i3+} = D_{3a}\frac{C_{O_2}^a - C_{O_2}^{i3}}{h_g} \quad , \tag{A30}$$

$$J_3^{O_2,i3-} = D_{23}\frac{C_{O_2}^{i3} - C_{O_2}^{i2}}{h_{ox}} f_g \quad , \tag{A31}$$

where D_{23} and D_{3a} are the oxygen diffusivity in the region (2–3) and region (3–a), respectively. Since B_2O_3 evaporates much faster than SiO_2 at the surface, the glassy layer contains more SiO_2 than borosilicate filled in the porous channels. As a result, the diffusivity for oxygen in region (2–3) is different from that in region (3–a). $C_{O_2}^{i3}$ and $C_{O_2}^a$ are the oxygen concentration at the interface 3 and a, respectively. $C_{O_2}^a$ is expressed as

$$C_{O_2}^a = p_{O_2}^a S \quad , \tag{A32}$$

where $p_{O_2}^a$ and S are the oxygen partial pressure at the air interface and solubility of oxygen in the glassy borosilicate.

Substituting Eqs. (A30) and (A31) into Eq. (A29), we obtain

$$C_{O_2}^{i3} = \frac{D_{3a}h_{ox}C_{O_2}^a + D_{23}f_g h_g C_{O_2}^{i2}}{D_{23}f_g h_g + D_{3a}h_{ox}} \quad , \tag{A33}$$

and then we get the oxygen flux at the moving boundary

$$J_3^{O_2,i2} = D_{23}f_g\frac{C_{O_2}^{i3} - C_{O_2}^{i2}}{h_{ox}} \quad . \tag{A34}$$

Solving Eqs. (A27), (A33), and (A34) simultaneously, we obtain the oxygen concentration at the interface 2, $C_{O_2}^{i2}$.

Accompanying the oxide layer growth, the stress is produced. Based on Clarke's assumption,[44,71] the lateral growth strain is proportional to the oxide layer thickness.

$$\varepsilon_{ox}^g = D_{ox}h_{ox} \quad , \tag{A35}$$

where D_{ox} is the lateral growth coefficient.

The elastic strain is

https://doi.org/10.1557/jmr.2016.489 Published online by Cambridge University Press

$$\varepsilon_i^{\mathrm{e}} = \frac{1-v_i}{E_i}\sigma_i \quad , \tag{A36}$$

where i can be replaced by ox for oxide and sub for substrate. ν_i, E_i, and σ_i are the Poisson ratio, Young's modulus and plane stress, respectively.

For the porous oxide layer, the relationship between Yong's modulus and porosity is[61]

$$E_{\mathrm{ox}} = \frac{E_{\mathrm{ox}}^0}{1+\frac{4f_{\mathrm{g}}\left(1-v_{\mathrm{ox}}^2\right)}{\pi}} \quad , \tag{A37}$$

where E_{ox}^0 is the Yong's modulus of oxide when there is no pore.

For the high-temperature oxidation, the creep effect should be taken into account. Here, Norton's creep power law[72] is adopted in the work.

$$\dot{\varepsilon}_i^c = \mathrm{sign}(\sigma_i) B_i \exp\left(-\frac{Q_i}{RT}\right)|\sigma_i|^{n_i} \quad , \tag{A38}$$

where B, Q, and n are the material constant, activation energy for creep process and the stress exponent, respectively. Since the stress is compressive in the oxide layer and tensile in the substrate, $\mathrm{sign}(\sigma_{\mathrm{ox}}) = -1$ and $\mathrm{sign}(\sigma_{\mathrm{sub}}) = 1$.

The total strain in the oxide and substrate is expressed, respectively, as

$$\varepsilon_{\mathrm{ox}} = \varepsilon_{\mathrm{ox}}^{\mathrm{g}} + \varepsilon_{\mathrm{ox}}^{\mathrm{e}} + \varepsilon_{\mathrm{ox}}^{\mathrm{c}} \quad , \tag{A39}$$

$$\varepsilon_{\mathrm{sub}} = \varepsilon_{\mathrm{sub}}^{\mathrm{e}} + \varepsilon_{\mathrm{sub}}^{\mathrm{c}} \quad . \tag{A40}$$

For the cracking, bulking and spalling are not taken into account in the work, the strain in the oxide and substrate should be compatible.

$$\varepsilon_{\mathrm{ox}}^{\mathrm{g}} + \varepsilon_{\mathrm{ox}}^{\mathrm{e}} + \varepsilon_{\mathrm{ox}}^{\mathrm{c}} = \varepsilon_{\mathrm{sub}}^{\mathrm{e}} + \varepsilon_{\mathrm{sub}}^{\mathrm{c}} \tag{A41}$$

The rate of Eq. (A41) is

$$\dot{\varepsilon}_{\mathrm{ox}}^{\mathrm{g}} + \dot{\varepsilon}_{\mathrm{ox}}^{\mathrm{e}} + \dot{\varepsilon}_{\mathrm{ox}}^{\mathrm{c}} = \dot{\varepsilon}_{\mathrm{sub}}^{\mathrm{e}} + \dot{\varepsilon}_{\mathrm{sub}}^{\mathrm{c}} \quad . \tag{A42}$$

Substituting Eqs. (A35), (A36) and (A38) into Eq. (A42), we obtain

$$\begin{aligned} &D_{\mathrm{ox}}\dot{h}_{\mathrm{ox}} + \frac{1-v_{\mathrm{ox}}}{E_{\mathrm{ox}}}\dot{\sigma}_{\mathrm{ox}} - \frac{1-v_{\mathrm{ox}}}{E_{\mathrm{ox}}^2}\dot{E}_{\mathrm{ox}}\sigma_{\mathrm{ox}} \\ &-B_{\mathrm{ox}}\exp\left(-\frac{Q_{\mathrm{ox}}}{RT}\right)(-\sigma_{\mathrm{ox}})^{n_{\mathrm{ox}}} = \frac{1-v_{\mathrm{sub}}}{E_{\mathrm{sub}}}\dot{\sigma}_{\mathrm{sub}} \\ &+B_{\mathrm{sub}}\exp\left(-\frac{Q_{\mathrm{sub}}}{RT}\right)(\sigma_{\mathrm{sub}})^{n_{\mathrm{sub}}} \quad . \end{aligned} \tag{A43}$$

The force equilibrium equation is

$$\begin{aligned} &\int_{h_{\mathrm{ox}}} \sigma_{\mathrm{ox}}\,\mathrm{d}h + \int_{h_{\mathrm{sub}}} \sigma_{\mathrm{sub}}\,\mathrm{d}h = 0, \ \text{i.e.,} \ \sigma_{\mathrm{ox}}h_{\mathrm{ox}} \\ &+ \sigma_{\mathrm{sub}}h_{\mathrm{sub}} = 0 \quad , \end{aligned} \tag{A44}$$

where h_{sub} is the thickness of substrate. In the work, we deal with the average stress in the oxide and substrate. From Eq. (A44), σ_{sub} can be expressed as

$$\sigma_{\mathrm{sub}} = -\sigma_{\mathrm{ox}}h_{\mathrm{ox}}/h_{\mathrm{sub}} \quad . \tag{A45}$$

The rate of Eq. (A45) is

$$\dot{\sigma}_{\mathrm{sub}} = -\dot{\sigma}_{\mathrm{ox}}h_{\mathrm{ox}}/h_{\mathrm{sub}} - \sigma_{\mathrm{ox}}\frac{\dot{h}_{\mathrm{ox}}h_{\mathrm{sub}} - h_{\mathrm{ox}}\dot{h}_{\mathrm{sub}}}{h_{\mathrm{sub}}^2} \quad . \tag{A46}$$

Substituting Eqs. (A45) and (A46) into Eq. (A43), we obtain

$$\begin{aligned} &D_{\mathrm{ox}}\dot{h}_{\mathrm{ox}} + \frac{1-v_{\mathrm{ox}}}{E_{\mathrm{ox}}}\dot{\sigma}_{\mathrm{ox}} - \frac{1-v_{\mathrm{ox}}}{E_{\mathrm{ox}}^2}\dot{E}_{\mathrm{ox}}\sigma_{\mathrm{ox}} - B_{\mathrm{ox}}\exp\left(-\frac{Q_{\mathrm{ox}}}{RT}\right) \\ &(-\sigma_{\mathrm{ox}})^{n_{\mathrm{ox}}} \\ &= -\frac{1-v_{\mathrm{sub}}}{E_{\mathrm{sub}}}\left(\dot{\sigma}_{\mathrm{ox}}h_{\mathrm{ox}}/h_{\mathrm{sub}} + \sigma_{\mathrm{ox}}\frac{\dot{h}_{\mathrm{ox}}h_{\mathrm{sub}} - h_{\mathrm{ox}}\dot{h}_{\mathrm{sub}}}{h_{\mathrm{sub}}^2}\right) \\ &+B_{\mathrm{sub}}\exp\left(-\frac{Q_{\mathrm{sub}}}{RT}\right)(-\sigma_{\mathrm{ox}}h_{\mathrm{ox}}/h_{\mathrm{sub}})^{n_{\mathrm{sub}}} \quad . \end{aligned} \tag{A47}$$

Rearranging Eq. (A47), we get

$$\begin{aligned} \dot{\sigma}_{\mathrm{ox}} = &\left[B_{\mathrm{ox}}\exp\left(-\frac{Q_{\mathrm{ox}}}{RT}\right)(-\sigma_{\mathrm{ox}})^{n_{\mathrm{ox}}} + B_{\mathrm{sub}}\exp\left(-\frac{Q_{\mathrm{sub}}}{RT}\right)(-\sigma_{\mathrm{ox}}h_{\mathrm{ox}}/h_{\mathrm{sub}})^{n_{\mathrm{sub}}}\right. \\ &\left.+\left(\frac{1-v_{\mathrm{ox}}}{E_{\mathrm{ox}}^2}\dot{E}_{\mathrm{ox}} - \frac{1-v_{\mathrm{sub}}}{E_{\mathrm{sub}}}\frac{\dot{h}_{\mathrm{ox}}h_{\mathrm{sub}} - h_{\mathrm{ox}}\dot{h}_{\mathrm{sub}}}{h_{\mathrm{sub}}^2}\right)\sigma_{\mathrm{ox}} - D_{\mathrm{ox}}\dot{h}_{\mathrm{ox}}\right] \Big/ \\ &\left(\frac{1-v_{\mathrm{ox}}}{E_{\mathrm{ox}}} + \frac{1-v_{\mathrm{sub}}}{E_{\mathrm{sub}}}h_{\mathrm{ox}}\Big/h_{\mathrm{sub}}\right) \quad . \end{aligned} \tag{A48}$$

In the same way, we get

$$\begin{aligned} \dot{\sigma}_{\mathrm{sub}} = &\left[B_{\mathrm{ox}}\exp\left(-\frac{Q_{\mathrm{ox}}}{RT}\right)(\sigma_{\mathrm{sub}}h_{\mathrm{sub}}/h_{\mathrm{ox}})^{n_{\mathrm{ox}}} + B_{\mathrm{sub}}\exp\left(-\frac{Q_{\mathrm{sub}}}{RT}\right)(\sigma_{\mathrm{sub}})^{n_{\mathrm{sub}}}\right. \\ &+\left(\frac{1-v_{\mathrm{ox}}}{E_{\mathrm{ox}}}\frac{\dot{h}_{\mathrm{sub}}h_{\mathrm{ox}} - h_{\mathrm{sub}}\dot{h}_{\mathrm{ox}}}{h_{\mathrm{ox}}^2} - \frac{1-v_{\mathrm{ox}}}{E_{\mathrm{ox}}^2}\dot{E}_{\mathrm{ox}}h_{\mathrm{sub}}\Big/h_{\mathrm{ox}}\right)\sigma_{\mathrm{sub}} \\ &\left.-D_{\mathrm{ox}}\dot{h}_{\mathrm{ox}}\right]\Big/\left(-\frac{1-v_{\mathrm{ox}}}{E_{\mathrm{ox}}}h_{\mathrm{sub}}\Big/h_{ox} - \frac{1-v_{\mathrm{sub}}}{E_{\mathrm{sub}}}\right) \quad . \end{aligned} \tag{A49}$$

The equations can be calculated by the evolutionary algorithm by assuming an initial thickness of h_{ox} and h_{g}.

The variation of pore radius r and borosilicate volume fraction f_{g} is

$$r = r^0\left(1+\varepsilon_{\mathrm{pore}}\right) \quad , \tag{A50}$$

$$f_{\mathrm{g}} = f_{\mathrm{g}}^0\left(1+\varepsilon_{\mathrm{pore}}\right)^2 \quad , \tag{A51}$$

where r^0 and f_{g}^0 are the pore radius and glassy borosilicate volume fraction when there is no stress.

https://doi.org/10.1557/jmr.2016.489 Published online by Cambridge University Press

The relationship between the macroscopic strain and the microscopic strain in the pore is expressed as[73]

$$\boldsymbol{\varepsilon}_{\text{pore}} = (\mathbf{I} - \mathbf{S})^{-1} : \mathbf{E} \quad , \tag{A52}$$

where $\mathbf{I}$ is the forth-order identity tensor. $\mathbf{S}$ is the Eshelby tensor. $\mathbf{E}$ is the macroscopic strain. If the effect of lateral growth strain on the pore strain is neglected, the pore strain is

$$\boldsymbol{\varepsilon}_{\text{pore}} = (\mathbf{I} - \mathbf{S})^{-1} : \left(\boldsymbol{\varepsilon}^{\text{e}}_{\text{ox}} + \boldsymbol{\varepsilon}^{\text{c}}_{\text{ox}}\right) \quad . \tag{A53}$$

To implement the model, the equations can be rewritten in incremental forms with respect to incremental time, Δt. Eqs. (A24) and (A25) are rewritten as

$$\Delta h_{\text{ox}} = \frac{V_{\text{ZrO}_2}}{f_{\text{ZrO}_2}} k_1^0 \exp\left(\frac{\eta_{\text{p}} V_{\text{m}} \sigma_{kk}}{RT}\right) \left(C^{i2}_{\text{O}_2}\right)^{5/2} \Delta t \quad , \tag{A54}$$

$$\begin{aligned}\Delta h_{\text{g}} = &\left[k_1^0 \exp\left(\frac{\eta_{\text{p}} V_{\text{m}} \sigma_{kk}}{RT}\right) \left(C^{i2}_{\text{O}_2}\right)^{5/2} - \left|J_{\text{B}_2\text{O}_3-\text{vap}}\right|\right] V_{\text{B}_2\text{O}_3} \Delta t \\ &+ \left[\frac{5}{3}\frac{f_{\text{s}}}{1-f_{\text{s}}} k_1^0 \exp\left(\frac{\eta_{\text{p}} V_{\text{m}} \sigma_{kk}}{RT}\right) \left(C^{i2}_{\text{O}_2}\right)^{5/2} \right. \\ &\left. - \left|J_{\text{SiO}_2-\text{vap}}\right| - \left|J_{\text{SiO}-\text{vap}}\right|\right] V_{\text{SiO}_2} \Delta t - \Delta h_{\text{ox}} f_{\text{g}} \quad . \end{aligned} \tag{A55}$$

The thickness at $t^{(k+1)}$ can be easily obtained as

$$h_{\text{ox}}^{(k+1)} = h_{\text{ox}}^{(k)} + \Delta h_{\text{ox}} \quad , \tag{A56}$$

$$h_{\text{g}}^{(k+1)} = h_{\text{g}}^{(k)} + \Delta h_{\text{g}} \quad . \tag{A57}$$

In the same way, Eqs. (A48) and (A49) are rewritten as

$$\begin{aligned}\Delta\sigma_{\text{ox}} = &\left[B_{\text{ox}} \exp\left(-\frac{Q_{\text{ox}}}{RT}\right) \left(-\sigma_{\text{ox}}^{(k)}\right)^{n_{\text{ox}}} \Delta t + B_{\text{sub}} \exp\left(-\frac{Q_{\text{sub}}}{RT}\right) \right. \\ &\left(-\sigma_{\text{ox}}^{(k)} h_{\text{ox}}^{(k)} \Big/ h_{\text{sub}}^{(k)}\right)^{n_{\text{sub}}} \Delta t + \left(\frac{1-\nu_{\text{ox}}}{E_{\text{ox}}^2} \Delta E_{\text{ox}} \right. \\ &\left. \left. - \frac{1-\nu_{\text{sub}}}{E_{\text{sub}}} \frac{\Delta h_{\text{ox}} h_{\text{sub}}^{(k)} - h_{\text{ox}}^{(k)} \Delta h_{\text{sub}}}{\left(h_{\text{sub}}^{(k)}\right)^2}\right) \sigma_{\text{ox}}^{(k)} - D_{\text{ox}} \Delta h_{\text{ox}}\right] \Big/ \\ &\left(\frac{1-\nu_{\text{ox}}}{E_{\text{ox}}} + \frac{1-\nu_{\text{sub}}}{E_{\text{sub}}} h_{\text{ox}}^{(k)} \Big/ h_{\text{sub}}^{(k)}\right) \quad , \end{aligned} \tag{A58}$$

$$\begin{aligned}\Delta\sigma_{\text{sub}} = &\left[B_{\text{ox}} \exp\left(-\frac{Q_{\text{ox}}}{RT}\right) \left(\sigma_{\text{sub}}^{(k)} h_{\text{sub}}^{(k)} \Big/ h_{\text{ox}}^{(k)}\right)^{n_{\text{ox}}} \Delta t \right. \\ &+ B_{\text{sub}} \exp\left(-\frac{Q_{\text{sub}}}{RT}\right) \left(\sigma_{\text{sub}}^{(k)}\right)^{n_{\text{sub}}} \Delta t \\ &\left. + \left(\frac{1-\nu_{\text{ox}}}{E_{\text{ox}}} \frac{\Delta h_{\text{sub}} h_{\text{ox}}^{(k)} - h_{\text{sub}}^{(k)} \Delta h_{\text{ox}}}{\left(h_{\text{ox}}^{(k)}\right)^2} - \frac{1-\nu_{\text{ox}}}{E_{\text{ox}}^2} \Delta E_{\text{ox}} h_{\text{sub}}^{(k)} \Big/ h_{\text{ox}}^{(k)}\right) \sigma_{\text{sub}}^{(k)} \right. \\ &\left. - D_{\text{ox}} \Delta h_{\text{ox}}\right] \Big/ \left(-\frac{1-\nu_{\text{ox}}}{E_{\text{ox}}} h_{\text{sub}}^{(k)} \Big/ h_{\text{ox}}^{(k)} - \frac{1-\nu_{\text{sub}}}{E_{\text{sub}}}\right) \quad . \end{aligned} \tag{A59}$$

The stress at $t^{(k+1)}$ can be easily obtained as

$$\sigma_{\text{ox}}^{(k+1)} = \sigma_{\text{ox}}^{(k)} + \Delta\sigma_{\text{ox}} \quad , \tag{A60}$$

$$\sigma_{\text{sub}}^{(k+1)} = \sigma_{\text{sub}}^{(k)} + \Delta\sigma_{\text{sub}} \quad . \tag{A61}$$

https://doi.org/10.1557/jmr.2016.489 Published online by Cambridge University Press